



Natural bentorite—Cr³⁺ derivate of ettringite: determination of crystal structure

Yurii V. Seryotkin^{1,2} · Ella V. Sokol¹ · Svetlana N. Kokh¹ · Victor V. Sharygin^{1,2}

Received: 24 July 2018 / Accepted: 14 January 2019 / Published online: 28 January 2019
© Springer-Verlag GmbH Germany, part of Springer Nature 2019

Abstract

Bentorite, a Cr³⁺-substituted analogue of ettringite (Ca₆Cr₂(SO₄)₃(OH)₁₂·26H₂O), has been found as veinlet filling at its holotype locality in the Hatrurim Basin (Negev Desert). Quite abundant massive bentorite with Cr/(Cr + Al) ratios up to 0.95–0.99 coexists with sporadic portlandite, gypsum, afwillite, truscottite, fluorapatite, tobermorite, calcite, and vaterite. It occurs as almost monomineralic clots composed of fibrous grains. The crystal structure of bentorite has been determined and refined for the first time by XRD powder diffraction coupled with high-accuracy synchrotron low-temperature measurements at 100, 250 K and 295 K. Bentorite is isostructural with ettringite, space group *P31c*. The analysed bentorite sample has a trigonal unit cell with the parameters $a = 11.16150(5)$, $c = 21.63017(19)$ Å, $V = 2333.650(19)$ Å³ at 100 K; $a = 11.17790(5)$, $c = 21.7375(2)$ Å, and $V = 2352.12(2)$ Å³ at 250 K, and $a = 11.2110(2)$, $c = 21.7654(7)$ Å, and $V = 2369.10(7)$ Å³ at 295 K. The bentorite structure includes only (SO₄)²⁻-groups, three anions per formula unit, as in ettringite. Unlike ettringite, bentorite has Cr³⁺ instead of Al³⁺ cations, this being the only difference in chemistry. The obtained structure confirms the existence of a continuous series of ettringite Ca₆Al₂^M[SO₄]₃^R(OH)₁₂·26H₂O–bentorite Ca₆Cr₂^M[SO₄]₃^R(OH)₁₂·26H₂O solid solutions over the whole range $0 \leq \text{Cr}^{3+}/(\text{Al} + \text{Cr}^{3+}) \leq 1$.

Keywords Bentorite · Crystal structure · Bentorite–ettringite solid solutions · Chromium

Introduction

The ettringite group consists of highly hydrated hexagonal or trigonal basic salts with the general formula Ca₆M₂(OH)₁₂R_{3–4}·*n*H₂O, where M = Al³⁺, Cr³⁺, Fe³⁺, Si⁴⁺, Mn⁴⁺ or Ge⁴⁺ is species-forming cation and R = (SO₄)²⁻, (CO₃)²⁻, (CrO₄)²⁻, (SO₃)²⁻, (PO₃OH)²⁻, or (B(OH)₄)⁻ is species-forming anionic group. Ettringite group minerals are important industrial compounds, but are rare in natural occurrence because a combination of nontrivial conditions is required for their formation and survival: low temperature

($T < 100$ °C), high alkalinity (pH = 9.5–13), and high humidity (Pöllmann et al. 1989, 1993; Pöllmann and Kuzel 1990; Perkins and Palmer 1999; Goetz-Neunhoeffler et al. 2006; Terai et al. 2006; Möschner et al. 2009; Pekov et al. 2012; Chukanov et al. 2018; Seryotkin et al. 2018). Upon contact with meteoric agents, sulphate varieties of ettringite often become replaced first by thaumasite and then by calcium carbonates and gypsum.

The Cr³⁺-substituted analogue of ettringite likewise can form in a very particular environment of highly alkaline (pH = 9.5–12.2) and Cr³⁺-rich (0.003–0.037 mol/dm³) solutions (Wieczorek-Ciurowa et al. 2001). All findings of natural Cr³⁺- and (CrO₄)²⁻-substituted ettringites have been in the vicinity of the Dead Sea within their type locality, the so-called Mottled Zone or the Hatrurim Formation complexes (Gross 1980; Hauff et al. 1983; Sokol et al. 2011; Drebuschak et al. 2013; Liu et al. 2017; Seryotkin et al. 2018). Cr³⁺-substituted ettringite was sampled for the first time in 1978 at the marble factory of Kibbutz Sedom Yam (Israel) and then by Sh. Gross (1980) near the Arad-Sedom road (Negev Desert) within the largest Mottled Zone complex of the Hatrurim Basin. Gross defined

Electronic supplementary material The online version of this article (<https://doi.org/10.1007/s00269-019-01022-4>) contains supplementary material, which is available to authorized users.

✉ Svetlana N. Kokh
s.n.kokh@gmail.com; zateeva@igm.nsc.ru

¹ Sobolev Institute of Geology and Mineralogy, Siberian Branch of the Russian Academy of Sciences, 3 Koptyug Avenue, Novosibirsk 630090, Russia

² Novosibirsk State University, 2 Pirogov Street, Novosibirsk 630090, Russia

the mineral as Cr^{3+} derivate of ettringite and described it as bentorite, a new mineral species. Bentorite has been found nowhere else since then (Liu et al. 2017), though it can be easily spotted due to its bright lilac coloration.

The composition of the bentorite holotype sample was determined by atomic absorption spectrometry and differential thermal analysis, in a hand-picked concentrate, pure to ~80% (Gross 1980). Extracting a monomineralic fraction was impossible because bentorite occurred as fibrous masses, rosettes of fine needles, and granular aggregates tightly intergrown with calcite and truscottite ($\text{Ca}_{14}\text{Si}_{24}\text{O}_{58}(\text{OH})_8 \cdot 2\text{H}_2\text{O}$). The concentrate contained 29.90 wt% CaO, in excess of the stoichiometric concentration, as well as 6.70 wt% CO_2 and 2.50 wt% SiO_2 . The residue after extraction of CO_2 and excess CaO as calcite and SiO_2 , CaO and H_2O as ideal truscottite led to the empirical formula $\text{Ca}_{5.88}(\text{Cr}_{1.61}\text{Al}_{0.32}\text{Fe}^{3+}_{0.02})_{\Sigma 1.95}\text{S}_{3.06}\text{O}_{18} \cdot 34.04\text{H}_2\text{O}$ (or $\text{Ca}_{5.88}(\text{Cr}_{1.61}\text{Al}_{0.32}\text{Fe}^{3+}_{0.02})_{\Sigma 1.95}\text{S}_{3.06}\text{O}_{18}(\text{OH})_{12} \cdot 26\text{H}_2\text{O}$ in a later form complying with the actual IMA nomenclature). Thus, the presence of $(\text{CO}_3)^{2-}$ groups and Si in the bentorite holotype sample remained unclear.

Gross (1980) provided a BSE image of a relatively large bentorite crystal (~150 × 25 μm) with hexagonal prism $\{10\bar{1}0\}$, pyramid $\{10\bar{1}0\}$ (dipyramid according to Gross (1980)), and monohedral $\{0001\}$ or $\{000\bar{1}\}$ faces (identified by Gross (1980) as pinacoid). However, the bentorite crystals from the holotype sample were too small for X-ray single crystal analyses with the instrumental facilities of that time. Therefore, the unit cell parameters ($a = 22.35 \text{ \AA}$ and $c = 21.41 \text{ \AA}$) were determined on the basis of X-ray powder diffraction patterns with 32 reflections (Gross 1980). The space group ($P6_3/mmc$) was not determined directly but was assigned to bentorite by analogy with that of ettringite based on wrong early data of Bannister et al. (1936).

The structure of a synthetic Cr^{3+} -substituted analogue of ettringite likewise remains unrefined. One reason is that synthesis of single-phase Cr^{3+} -ettringite is problematic because it commonly forms along with other solids, such as gypsum, portlandite and $\text{Cr}(\text{OH})_3$ (Wieczorek-Ciurowa et al. 2001). On the other hand, the presence of Cr^{3+} changes dramatically the morphology of synthetic grains, namely clusters of very thin long needles of Cr^{3+} -rich ettringite form instead of relatively large (15–20 × 250 μm) long-prismatic crystals typical of ettringite (Cody et al. 2004). Cr^{3+} -ettringite synthesised from chloride solutions forms aggregates of fine stubby crystals (up to 0.3 μm) (Ogawa and Roy 1982; You et al. 2007).

This paper presents results of an X-ray powder diffraction study and Rietveld structure determination of natural bentorite from the Hatrurim Basin (Negev Desert).

Bentorite and Cr-bearing ettringites from the Mottled Zone complexes

The term Mottled Zone (MZ) sequence refers to diverse exposed and near-surface sedimentary rocks which underwent post-depositional alteration under highly contrasting conditions. The section consists of unevenly distributed brecciated sediments (mainly chalk that encloses phosphorite, chert, and marl) strongly altered by low-temperature alkaline aqueous solutions and cut by veinlets of calcite, aragonite, gypsum, various Ca silicate hydrates (CSHs), zeolite, and ettringite. The upper part of the section also includes numerous foci of anhydrous high- to ultrahigh-temperature combustion metamorphic rocks. The local geology, rock compositions, and possible formation mechanisms of the Mottled Zone complexes have been discussed in many publications (Bentor et al. 1963; Kolodny and Gross 1974; Khoury and Nassir 1982; Burg et al. 1991, 1999; Gilat 1998; Sokol et al. 2010, 2014; Novikov et al. 2013; Khoury et al. 2016; Sharygin 2019). Chromium mineralization and its sources for sedimentary parent rocks have been exhaustively characterised as well (Gross 1977, 1980; Khoury et al. 1984; Elie et al. 2007; Sokol et al. 2011; Fleurance et al. 2013; Khoury and Al-Zoubi 2014; Seryotkin et al. 2018). All these issues remain beyond the present consideration, which focuses exclusively on the crystal structure of natural bentorite.

During our field and laboratory studies of the Mottled Zone rocks since 2004, we have looked for bentorite crystals like those described by Gross (1980), which would be suitable for single-crystal XRD analysis. We failed to find any, though found $(\text{CrO}_4)^{2-}$ -bearing ettringite in the Nabi Musa area in Judean Desert (Sokol et al. 2011). Later on, quite abundant large perfect crystals of ettringite-bentorite solid solutions were discovered in the Ma'aleh Adumim area (Judean Desert), in crack filling from altered larnite rocks (Seryotkin et al. 2018). The Cr^{3+} -bearing ettringite occurred as druses of pinkish crystals, their intergrowths, and twins with monohedral terminations. The most typical pencil-like crystals with the aspect (length-to-width) ratios $L/W \sim 1.5\text{--}3$ had $\text{Cr}/(\text{Cr} + \text{Al}) = 0.1\text{--}0.2$.

Some pink long-prismatic crystals (to 300–500 μm long, $L/W \sim 5$) had hexagonal pyramidal $\{10\bar{1}1\}$ terminations and seemed identical to bentorite crystals described by Gross (1980) (Fig. 1). Their colour varied from pale pinkish at the base to bright pink at the pyramid-faceted top, and the $\text{Cr}/(\text{Cr} + \text{Al})$ ratio varied correspondingly from 0.23 at the base (monohedral growth sector, $\{0001\}$ or $\{000\bar{1}\}$) to 0.4–0.5 at 25–50 μm near the top (pyramidal growth sector) (Seryotkin et al. 2018). Small (20–75 × 4–15 μm) pink later crystals with $\text{Cr}/(\text{Cr} + \text{Al}) \sim 0.4$ growing chaotically over earlier coarse grains had the same L/W ratio ~5.

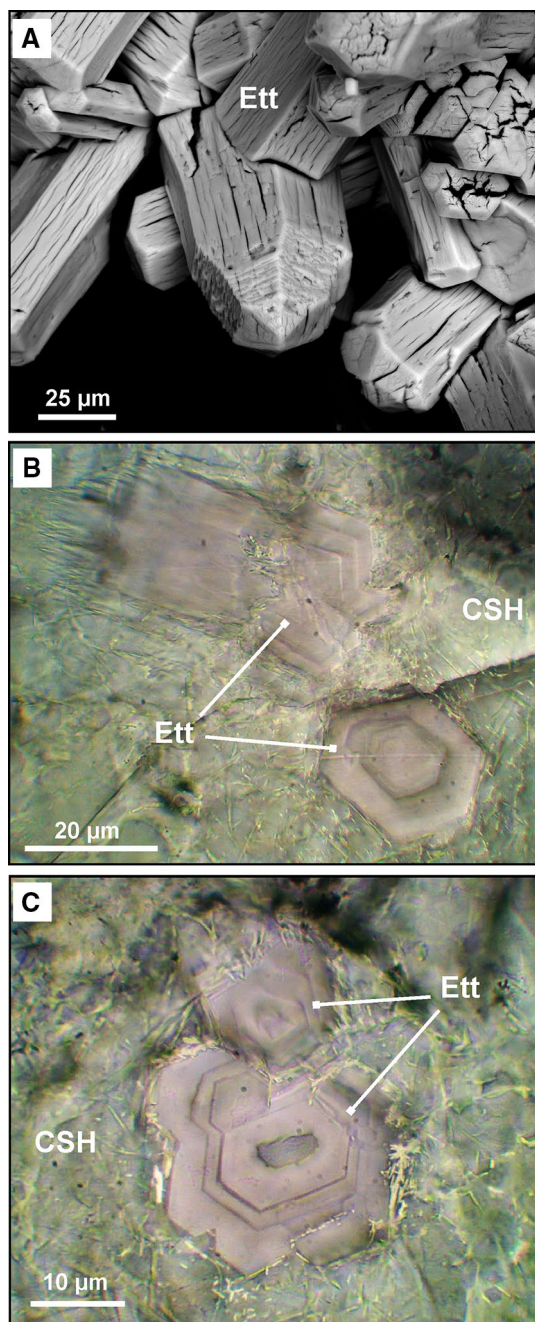


Fig. 1 Crystal morphology of Cr^{3+} -rich ettringite: BSE (a) and optical (b, c) images. b, c Plane-polarised light images. Mineral names are abbreviated as CSH Ca silicate hydrates, Ett Cr^{3+} -bearing ettringite

Commonly, hexagonal pyramidal faces (namely $\{10\bar{1}1\}$) become predominant over the $\{0001\}$ monohedral one at $\text{Cr}/(\text{Cr} + \text{Al}) \geq 0.4$ (Fig. 1a). This morphological criterion can be used for reference in preliminary visual examination of ettringites with high Cr^{3+} contents. Double-terminated crystals of Cr^{3+} -rich ettringite are hemimorphic

(Fig. 1b), that is, the opposite ends of their L_3 axes are not formed by the same faces (Seryotkin et al. 2018). In this respect, Cr-rich ettringites are analogous to tourmaline, a known representative of non-centrosymmetric trigonal hemihedral minerals (Deer et al. 1986).

None out of the analysed tens of pink crystals with this habit corresponds to the bentorite composition. As indicated by single-crystal XRD analyses, the Cr^{3+} -rich ettringite variety can retain the ettringite symmetry (Seryotkin et al. 2018). Many bright pink crystals corresponding to the composition of Cr^{3+} -rich ettringite have oscillation zonation according to Cr contents (Figs. 1b, c, 2a, b).

In general, samples from different Mottled Zone localities showed an appropriate trend of crystal morphology changes with increasing Cr^{3+} up to the bentorite composition (Fig. 2). At $\text{Cr}/(\text{Cr} + \text{Al}) \geq 0.5$, aggregates of thin prismatic crystals ($L/W > 10$) grown together along the c -axis, as well as split or curved crystals, form instead of single crystals and simple twins. Bentorite ($\text{Cr}/(\text{Cr} + \text{Al}) \geq 0.8$) occasionally occurs as fibrous radial crystal aggregates with $L/W > 50$ or as clots (Figs. 2, 3).

Earlier we (Sokol et al. 2011) found a mineral corresponding to the Cr^{3+} -substituted end member $(\text{Ca}_6\text{Cr}_{1.99}\text{Al}_{0.01}(\text{SO}_4)_3(\text{OH})_{12} \cdot 26\text{H}_2\text{O})$ in the vicinity of Har Ye'elim mountain, northern Hatrurim Basin. Bentorite, prominent with its deep lilac colour, occurred as a main or abundant constituent in thin (2–6 mm wide) vug-free veinlets which cut the low-grade Hatrurim rocks mainly composed of calcite, CSHs, and gypsum. Bentorite frequently occupied the whole crack space (Fig. 3a), and was often intergrown with less abundant fine-grained portlandite, calcite, vaterite, CSHs (mainly afwillite), and fluorapatite; it also formed round nearly monomineralic clots composed of fibrous masses or granular aggregates (Fig. 3b).

Mineral chemistry of bentorite

As we previously found out with several methods, including thermogravimetric measurements of water content, the bulk chemistry of vein bentorite (Bent-1) corresponds to a Cr^{3+} end member (Sokol et al. 2011; Drebushchak et al. 2013). In this study, the ranges of element contents in bentorite were constrained using local microanalysis. Major oxide contents and analytical totals can be overestimated relative to the ideal composition, because bentorite, akin to many other ettringite group minerals (Thiéry et al. 2017; Chukanov et al. 2018), is unstable under the electron beam and dehydrates quickly in vacuum (Figs. 1a, 3c). Nevertheless, SEM–energy-dispersive spectroscopy (EDS) and EMPA analyses of dehydrated bentorite are well reproducible, fit the $\text{Ca}_6(\text{Cr}, \text{Al})_2(\text{SO}_4)_3(\text{OH})_{12}$ stoichiometry, and can be recalculated to the ideal formula

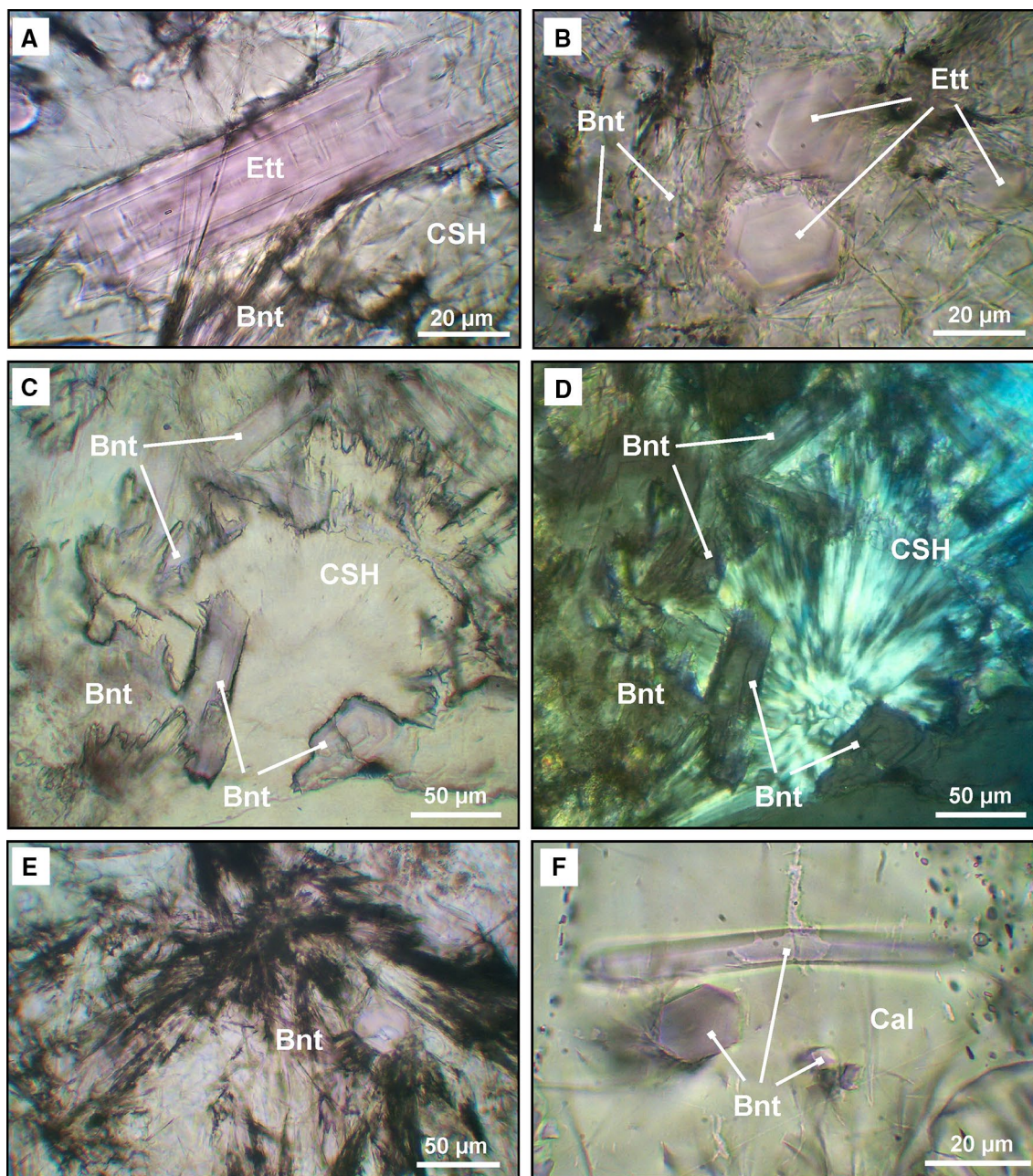


Fig. 2 Crystal morphology of Cr^{3+} -bearing ettringite and benterite from the Hatrurim Basin locality, Negev desert: optical images. **a** Long prism of Cr^{3+} -bearing ettringite with split basal faces ($L/W \sim 5$; $\text{Cr}/(\text{Cr} + \text{Al}) = 0.22$) coexisting with a radial aggregate of benterite fibres ($L/W > 10$; $\text{Cr}/(\text{Cr} + \text{Al}) = 0.75$) in a CSH matrix. **b** Cross section of prismatic Cr^{3+} -bearing ettringite ($\text{Cr}/(\text{Cr} + \text{Al}) = 0.22$) with weakly pronounced zonation. Benterite ($\text{Cr}/(\text{Cr} + \text{Al}) = 0.61$) occurs as anhedral grains. **c, d** Benterite ($\text{Cr}/(\text{Cr} + \text{Al}) = 0.96$) in a CSH

matrix: split prismatic crystals and parallel intergrown needles. **e** Typical radial aggregate of benterite fibres ($\text{Cr}/(\text{Cr} + \text{Al}) = 0.99$). **f** Sections along and across needle-like ($L/W = 11$) curved benterite crystals ($\text{Cr}/(\text{Cr} + \text{Al}) = 0.88$ and 0.98 , correspondingly) in a calcite matrix. Plane-polarised (**a–c, e, f**) and cross-polarised light (**d**) images. Mineral names are abbreviated as *Cal* calcite, *Bnt* benterite, *CSH* Ca silicate hydrates, *Ett* Cr^{3+} -bearing ettringite. Numerals refer to the $\text{Cr}/(\text{Cr} + \text{Al})$ ratio at a given grain point (from EMPA)

($\text{Ca}_6(\text{Cr,Al})_2(\text{SO}_4)_3(\text{OH})_{12} \cdot 26\text{H}_2\text{O}$) to a satisfactory accuracy (Table 1).

Preliminary semiquantitative data on the benterite composition were obtained by means of a *MIRA3-LMU* scanning electron microscope (Tescan Orsay Holding, Czech

Republic) with an *INCA Energy 450 + XMax 80* analyser (Oxford Instruments Nanoanalysis Ltd, UK) at the Analytical Center for multi-elemental and isotope research SB RAS (IGM, Novosibirsk). Polished thin sections ($300 \mu\text{m}$) and fresh cleavage surfaces were sputter coated with

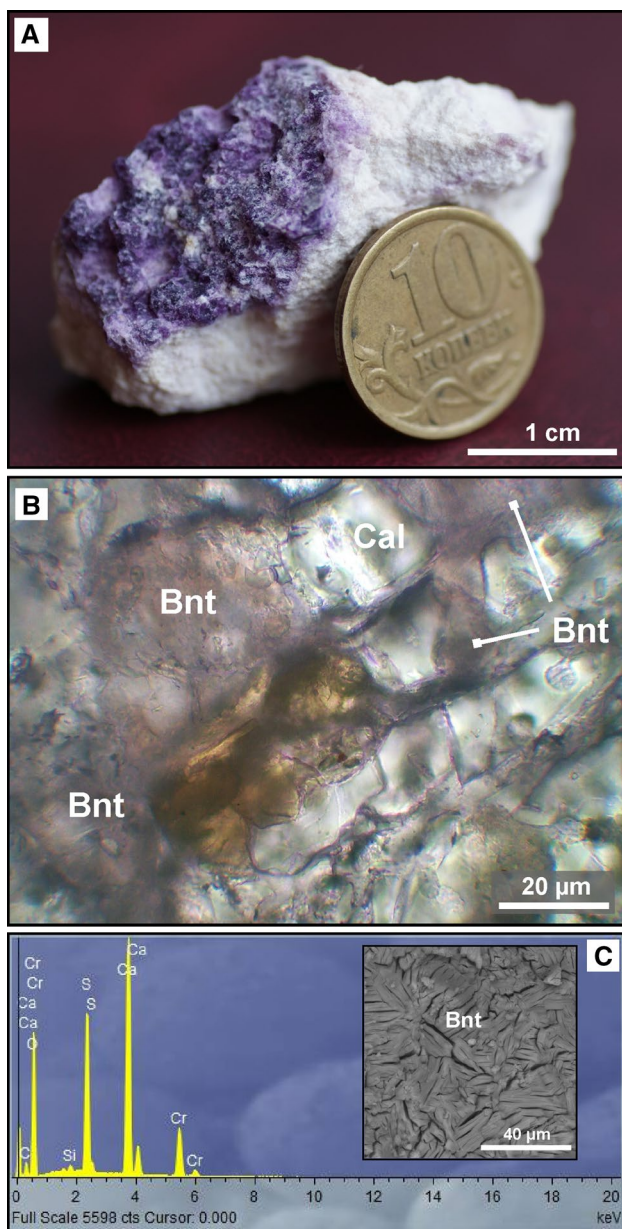


Fig. 3 Bentorite appearance (sample Bent-1). **a** Massive bentorite filling a vein in low-grade Hatrurim rocks. **b** Granular bentorite aggregate in thin section. Optical image, plane-polarised light. **c** BSE image and EDS spectrum of bentorite. Mineral names are abbreviated as *Cal* calcite, *Bnt* bentorite

~ 15–25 nm carbon films for SEM and EMPA examinations. EDS analyses were performed using an accelerating voltage of 10 kV, a beam current of 1.4 nA, and a small spot size (5–10 μm²) instead of a point probe (180 nm beam diameter), to minimise damage to the beam-sensitive samples. Relative percentages of major components in this dehydrated (but not dehydroxylated) material can be determined to a high accuracy, which was confirmed by single-crystal X-ray analysis of Cr³⁺-rich ettringites (Seryotkin

et al. 2018). EDS analysis is also highly informative for detection of main impurities. Only Ca, Cr, S, and O, as well as Al and/or Si impurities, were found to exceed detection limits in the analysed bentorites (Fig. 3c).

The bentorite mineral chemistry was additionally analysed by wavelength-dispersive EMPA in carbon-coated polished thin sections, on a JEOL JXA 8100 electron microprobe at IGM (Novosibirsk). The applied operation conditions of 20-keV accelerating voltage, 10-nA beam current, 5-s peak count time, and ~5 μm defocused beam allowed reducing beam damage to the vacuum-dehydrated samples; chamber vacuum was kept at 10⁻⁶ Torr (~0.001 Pa). Only > 20 μm particles were taken into consideration to avoid errors caused by the matrix capture. The compositions were estimated with reference to natural and synthetic standards: diopside (Ca, Mg and Si), chromium spinel UD-92 (Cr), K feldspar 359-1 (Al and K), CaSO₄ synth. (S), spessartine garnet IGM (Mn), pyrop-almandine garnet O-145 (Fe), Sr-Si glass G1-11 (Sr), albite synth. (Na). Matrix correction using the PAP routine was applied to raw data prior to recalculation into major oxides. The analytical accuracy was better than 2%-relative for > 5 wt% elements and about 5%-relative for ≤ 2 wt% elements.

The contents of major oxides determined by EMPA are bracketed within a narrow range between Ca₆Cr₂(SO₄)₃(OH)₁₂ and Ca₆(Cr_{1.8}Al_{0.2})(SO₄)₃(OH)₁₂: 39.73–40.49 wt% CaO; 16.75–17.36 wt% Cr₂O₃; 28.58–29.47 wt% SO₃; 0.16–1.12 wt% Al₂O₃; 0.16–0.59 wt% SiO₂; and 0.05–0.36 wt% FeO. The totals are deficient to 12–13 wt%. See Table 1 for the bentorite composition recalculated to the ideal formula (Ca₆(Cr,Al)₂(SO₄)₃(OH)₁₂·26H₂O).

To check the analytical results, the Bent-1 sample was reanalysed by a precise and non-destructive synchrotron radiation X-ray fluorescence (SR XRF) method with EDS, at 23-kV and 42-kV excitation, at the Siberian Synchrotron and Terahertz Radiation Center (SSTRC) based on laboratories of the Budker Institute of Nuclear Physics (Novosibirsk). For details of the method see Phedorin et al. (2000) and Sokol et al. (2014). The element abundances were measured in 50-mg fine powder (< 5 μm) specimens compressed into 6-mm pellets at 120–150 kg/cm². All measurements were run in three different pellets and quoted as averages. Recalculated to oxides, the contents of cations were 25.8 wt% CaO, 11.2 wt% Cr₂O₃, 0.21 wt% FeO, and 0.04 wt% MnO; alumina was not determined. The SR XRF data agree with the EDS–SEM and EMPA results and correspond to the bentorite end-member composition. Trace-element contents, determined by the same method, are 1100 ppm Sr, 123 ppm Zn, 21 ppm Se, 13 ppm As, and 5 ppm U.

Table 1 Representative analyses and average chemical composition of bentorite

	1	2	3	4	5	6	7	Aver. (<i>n</i> = 32)
<i>EMPA results (wt%)</i>								
SiO ₂	0.32	0.16	0.35	0.50	0.20	0.35	0.23	0.34
Cr ₂ O ₃	16.82	17.36	17.23	17.76	16.90	16.76	17.25	17.08
Al ₂ O ₃	1.12	0.09	0.30	0.28	0.20	0.26	0.16	0.34
FeO	0.18	0.05	0.12	0.05	0.09	0.36	0.04	0.13
MnO	0.06	0.06	0.12	0.07	0.10	0.07	0.08	0.07
MgO	0.03	0.01	0.03	0.09	0.00	0.02	0.00	0.02
CaO	40.46	40.38	40.53	40.25	40.04	40.16	40.49	40.25
SrO	0.06	0.10	0.08	0.08	0.10	0.07	0.07	0.08
Na ₂ O	0.00	0.00	0.02	0.01	0.01	0.00	0.00	0.01
K ₂ O	0.03	0.02	0.02	0.03	0.01	0.03	0.03	0.02
SO ₃	29.03	28.92	28.58	28.62	29.27	28.78	28.94	28.94
Total	88.10	87.14	87.37	87.73	86.92	86.84	87.30	87.28
<i>Normalised composition (wt%)</i>								
SiO ₂	0.20	0.10	0.22	0.32	0.13	0.22	0.15	0.22
Cr ₂ O ₃	10.68	11.11	10.99	11.33	10.87	10.77	11.01	10.93
Al ₂ O ₃	0.71	0.06	0.19	0.18	0.13	0.17	0.10	0.22
FeO	0.11	0.03	0.07	0.03	0.06	0.23	0.02	0.08
MnO	0.04	0.04	0.08	0.04	0.06	0.04	0.05	0.04
MgO	0.02	0.00	0.02	0.06	0.00	0.01	0.00	0.01
CaO	25.70	25.83	25.85	25.69	25.75	25.80	25.84	25.76
SrO	0.04	0.06	0.05	0.05	0.06	0.04	0.05	0.05
Na ₂ O	0.00	0.00	0.01	0.01	0.00	0.00	0.00	0.01
K ₂ O	0.02	0.01	0.01	0.02	0.01	0.02	0.02	0.01
SO ₃	18.44	18.50	18.23	18.27	18.82	18.49	18.47	18.52
H ₂ O ^a	44.04	44.26	44.28	44.01	44.11	44.21	44.28	44.14
Total	100.00	100.00	100.00	100.00	100.00	100.00	100.00	100.00
<i>Atoms p.f.u. based on 6 Ca atoms</i>								
Si	0.04	0.02	0.05	0.07	0.03	0.05	0.03	0.04
Cr	1.84	1.90	1.88	1.95	1.87	1.85	1.89	1.88
Al	0.18	0.01	0.05	0.05	0.03	0.04	0.03	0.06
Fe	0.02	0.01	0.01	0.01	0.01	0.04	0.00	0.01
Mn	0.01	0.01	0.01	0.01	0.01	0.01	0.01	0.01
Mg	0.01	0.00	0.01	0.02	0.00	0.00	0.00	0.01
Ca	6.00	6.00	6.00	6.00	6.00	6.00	6.00	6.00
Sr	0.00	0.00	0.00	0.00	0.00	0.00	0.00	0.00
Na	0.00	0.00	0.00	0.00	0.00	0.00	0.00	0.00
K	0.00	0.00	0.00	0.00	0.00	0.00	0.01	0.00
SO ₄	3.02	3.01	2.96	2.99	3.07	3.01	3.00	3.01
H ₂ O	26	26	26	26	26	26	26	26
OH	12	12	12	12	12	12	12	12

n Number of analyses

^aH₂O contents are calculated for ideal composition Ca₆M₂(SO₄)₃(OH)₁₂·26H₂O and was used for normalisation of EMPA data

Vibration spectroscopy

The Raman spectra of bentorite, ettringite, and Cr³⁺-rich ettringite reference samples were recorded on a Horiba Jobin

Yvon LabRAM HR800 spectrometer with a 1024 pixel LN/CCD detector using the 532-nm emission line of Nd laser, in the 0–4000 cm⁻¹ range, at a beam power of 1–5 mW, and a signal accumulation time of 30 min. The spectra were

collected in a back-scattering geometry, using an *Olympus BX41* microscope. The resolution of the recorded Stokes side of the spectra was set to 2 cm^{-1} at a Raman shift of $\sim 1000\text{ cm}^{-1}$, as achieved by grating with 1800 grooves/mm and equal $150\text{ }\mu\text{m}$ slit and pin hole sizes. The microscope with an *Olympus Plan 100X* objective lens of the working distance $\text{WD}=0.2\text{ mm}$ with 0.8 numerical aperture provides a focal spot diameter of $1\text{ }\mu\text{m}$ on the sample surface. The Raman spectra were deconvolved into Voigt amplitude functions using the *Model S506 Interactive PeakFit* software (2002).

Infrared spectra of bentorite were obtained by polarised Fourier-transform infrared (FTIR) spectroscopy using a *Bruker Vertex 70* spectrometer coupled with a *Hyperion 2000* microscope. Infrared radiation was polarised using a holographic wire grid polarizer on a ZnSe substrate (Optometrics Corporation, USA). Powdered bentorite samples were mixed with anhydrous KBr and pelletized. The spectra were acquired with a resolution of 2 cm^{-1} in the range $400\text{--}4000\text{ cm}^{-1}$ and averaged over 64 scans. FTIR spectra of similar pure KBr pellets were used for reference.

The Raman spectra of Cr-free and Cr^{3+} -rich ettringites and bentorite as well as the FTIR spectra of bentorite were interpreted with reference to experimental data for thaumasite (Brough and Atkinson 2001; Gatta et al. 2012), synthetic and natural ettringite (Myneni et al. 1998; Deb et al. 2003; Renaudin et al. 2007; Frost, 2013), as well as Al and Cr^{3+} -rich alums (Beattie and Best 1997; Tregenna-Piggott and Best 1996) and FTIR analyses of natural ettringite group minerals (Pekov et al. 2012; Frost et al. 2013; Chukanov 2014) and synthetic Cr^{3+} -substituted ettringite (You et al. 2007).

The Raman spectra of three studied minerals are generally similar. Ettringite and its Cr^{3+} -rich variety show the strongest band at 984 cm^{-1} (ν_1 symmetric stretching of the (SO_4) -group), which is shifted to 1000 cm^{-1} in the bentorite spectra (Fig. 4). Several bands at $400\text{--}500\text{ cm}^{-1}$ and a weak broad band at 1140 cm^{-1} are associated with the ν_2 symmetric bending and ν_3 symmetric stretching modes of the (SO_4) -group, respectively. The ν_4 (SO_4) stretching mode appears at 608 cm^{-1} .

The Raman spectra of all analysed ettringite group minerals contain prominent bands at $540\text{--}550\text{ cm}^{-1}$: a weak band at 548 cm^{-1} in ettringite, a medium band at 548 cm^{-1} in Cr^{3+} -rich ettringite, and a strong band at 540 cm^{-1} in bentorite. The 548-cm^{-1} band in the spectrum of Cr-free ettringite may represent $\text{Al}(\text{OH})_6$ vibration. Previously, bands at $555\text{--}542\text{ cm}^{-1}$ (Myneni et al. 1998) and 541 cm^{-1} (Renaudin et al. 2007) observed in the Raman spectra of synthetic ettringites were attributed to $\text{Al}(\text{OH})_6$ vibration in both publications. The stretching vibration modes of $\text{Al}(\text{OH})_6$ were also reported at 527 and 551 cm^{-1} (Deb et al. 2003) and at 546 cm^{-1} (Frost et al. 2013) for natural ettringites.

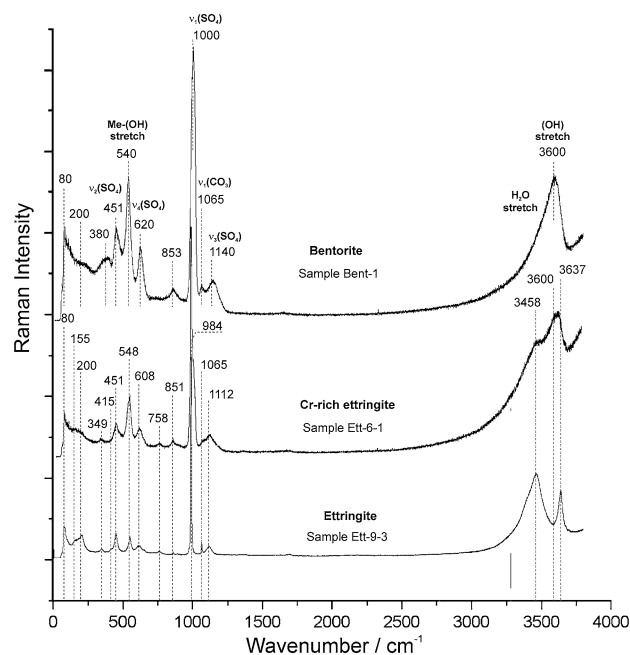


Fig. 4 Raman spectra of bentorite (sample Bent-1; $\text{Cr}/(\text{Cr}+\text{Al})\geq 0.85$), ettringite (sample Ett-9-3; $\text{Cr}/(\text{Cr}+\text{Al})<0.05$), and Cr-rich ettringite variety (sample Ett-6-1; $\text{Cr}/(\text{Cr}+\text{Al})=0.4\text{--}0.5$) were compared. Spectra of ettringites are after Seryotkin et al. (2018)

Since no published evidence was available for both synthetic and natural Cr^{3+} -substituted ettringites, we looked for their analogues among other Al- and Cr^{3+} -bearing water sulphates. The vibration modes between 540 and 550 cm^{-1} in the spectra of water sulphates are commonly attributed to trivalent hexaaqua cations (Beattie and Best 1997). These environments and coordinations are common to both Al^{3+} and Cr^{3+} in the ettringite structure (Fig. 5). In several alums, the symmetric stretching frequencies ν_1 ($\text{Me}(\text{OH})_6$) in $\text{Me}(\text{OH})_6$ units lie between 500 and 550 cm^{-1} (Beattie and Best 1997), while the $\nu_1(\text{MeO}_6)$ mode has similar wavenumbers in different alums (Tregenna-Piggott and Best 1996). It was found out that Cr^{3+} substitution for Al^{3+} in water sulphates led to shifting of the $\nu_1(\text{MeO}_6)$ mode to lower frequencies and to ~ 10 times greater intensity of the respective band (Tregenna-Piggott and Best 1996; Beattie and Best 1997). For instance, the wavenumbers of this mode in the spectra of rubidium alums $\text{RbMe}^{\text{III}}(\text{SO}_4)_2\cdot 12\text{H}_2\text{O}$ ($\text{Me}^{\text{III}} = \text{Al}, \text{Cr}$) are 545 cm^{-1} for $\nu_1(\text{AlO}_6)$ but 540 for $\nu_1(\text{CrO}_6)$. As Cr reaches 0.8 apfu, the ν_1 band in the spectrum of Cr^{3+} -bearing ettringite holds at 548 cm^{-1} but becomes four times stronger; the respective band in the bentorite spectrum is shifted to 540 cm^{-1} and is an order of magnitude stronger. Therefore, we suggest assigning the medium band at 548 cm^{-1} in the spectrum of Cr^{3+} -rich ettringite and the strong band at 540 cm^{-1} in that of bentorite to the symmetric

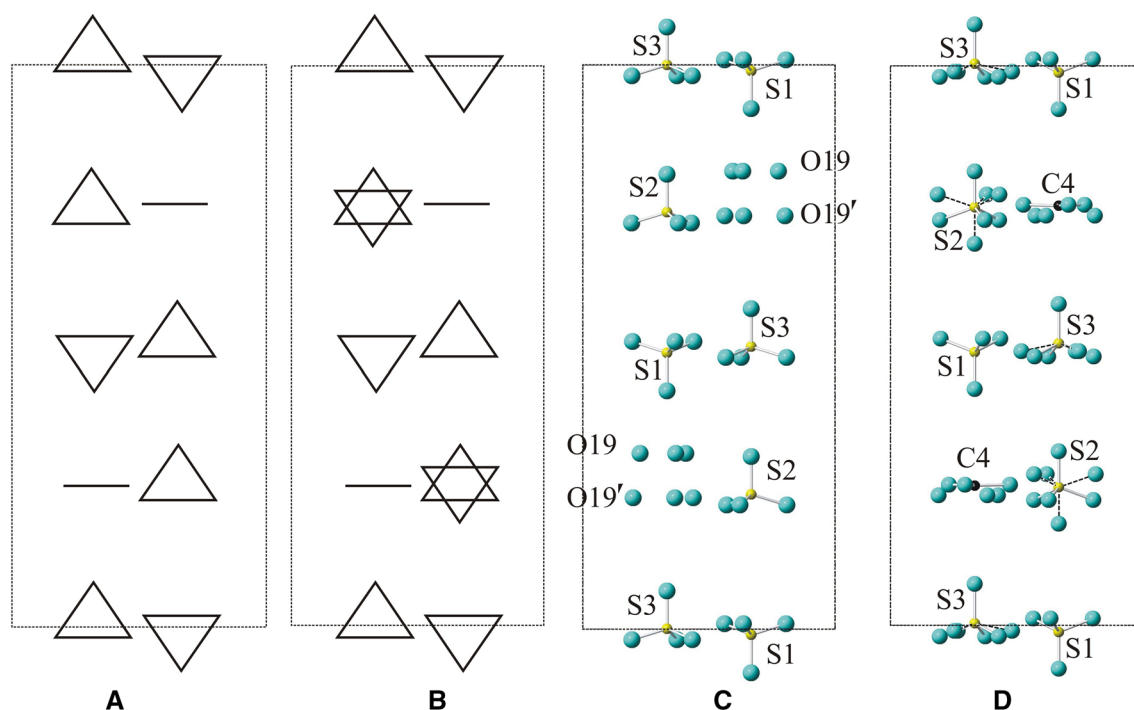


Fig. 5 Orientation of (SO₄)-groups in the ettringite structure: **a, b** space groups *P31c* and *P31c*, respectively (Moore and Taylor 1970); **c, d** Cr-free and Cr³⁺-rich ettringites, respectively (Seryotkin et al. 2018)

(MeO₆) stretching mode of hexaaquametal cations: Al³⁺ and Cr³⁺ for Cr³⁺-rich ettringite and Cr³⁺ for bentorite (Fig. 4).

It is yet impossible to reliably assign the weak but well pronounced ~850 cm⁻¹ band in the spectra of bentorite and Cr³⁺-rich ettringite to stretching vibrations of certain groups. Myneni et al. (1998) interpret it as Al-(OH) bending vibration, which implies that the intensity of this band corresponding to the Me(III)-(OH) bending vibration depends on the cation type, as in the case of $\nu_1(\text{MeO}_6)$: it is the strongest in the spectrum of Al-free bentorite but almost absent from that of ettringite. However, the same frequency range includes the $\nu_1 \text{Cr}^{6+}\text{O}_4$ symmetric stretching mode. As Frost (2004) reported, the Raman spectra of chromate minerals contain an intense band at ~840–848 cm⁻¹ in the CrO stretching region: at 841 cm⁻¹ in crocoite (PbCrO₄), at 840 cm⁻¹ in edoyleite (Hg²⁺₃Cr⁶⁺O₄S₂), and at 847 cm⁻¹ in fornacite (Pb₂Cu(AsO₄)(CrO₄)(OH)). Bentorite and Cr³⁺-rich ettringite may also contain minor amounts of (CrO₄)²⁻, but we failed to prove its presence with an independent method.

The weak band at 1065 cm⁻¹ is attributed to ν_1 symmetric stretching of the (CO₃)-group. No other ν_2 , ν_3 , or ν_4 modes of (CO₃)-group have been detected, which is evidence of their very low contents in all analysed minerals.

Several bands at 3300–3700 cm⁻¹ are associated with O–H stretching overtones (Myneni et al. 1998; Deb et al.

2003; Renaudin et al. 2007; Gatta et al. 2012). The intensity of the 3458 cm⁻¹ band in the spectrum of Cr³⁺-rich ettringite is much lower while the 3600–3640 cm⁻¹ band is broader and stronger than in the spectra of the other samples. The bentorite spectrum contains a single strong broad band at 3600 cm⁻¹ in this region. Thus, bentorite can be identified preliminarily from characteristic bands in its Raman spectrum.

The FTIR spectrum of natural bentorite is similar to that of ettringite (Deb et al. 2003; Pekov et al. 2012) (Fig. 6). The bentorite spectrum has a strong band at 1110 cm⁻¹, which is due to stretching vibrations of (SO₄)-groups. The bands at 1622 cm⁻¹ result from bending vibrations of H₂O molecules. The FTIR spectra of ettringite and bentorite are different in the 2800–3700 cm⁻¹ O–H-stretching region, where bentorite shows a strong broad band at 3421 + 3470 cm⁻¹ (a doublet ?) but ettringite has a single band with a sharp peak at 3440 cm⁻¹. A weak band at 3625 cm⁻¹ present in the ettringite spectrum is due to the Al(OH)₆ OH-stretching vibration (Deb et al. 2003) but is absent from the bentorite spectrum. A weak band at 1410 cm⁻¹ observed in the FTIR spectra of both ettringite and bentorite is due to stretching vibrations of (CO₃)²⁻ groups (Deb et al. 2003; Pekov et al. 2012). Earlier, You et al. (2007) detected a band at 785 cm⁻¹ in the FTIR spectrum of synthetic Cr³⁺-rich ettringite and

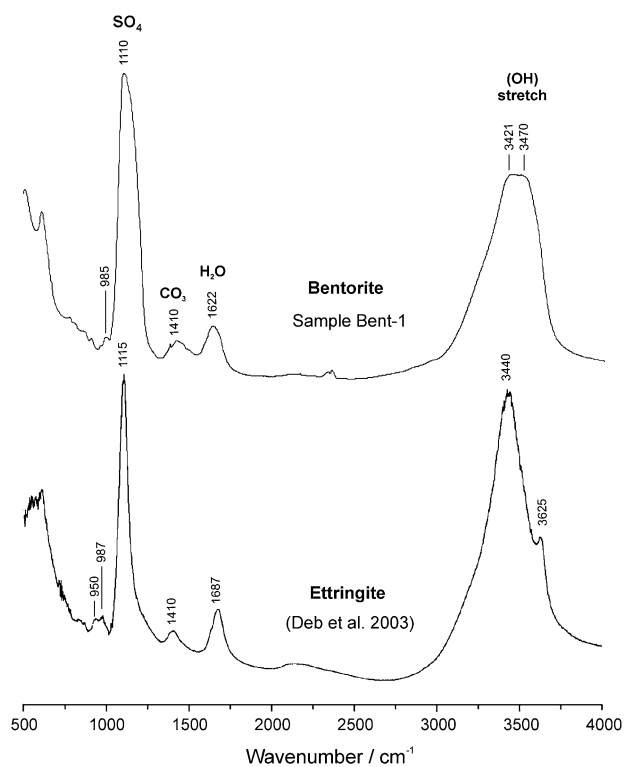


Fig. 6 FTIR spectra of bentorite (sample Bent-1) and ettringite (Deb et al. 2003)

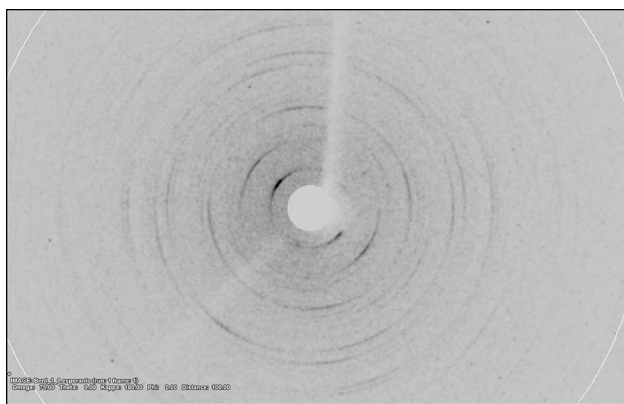


Fig. 7 2D frame collected in a single-crystal mode (ω -scan, step 1°). The position of Debye rings corresponds to diffraction peaks of bentorite. Weak single-crystal reflection belongs to associated minor phases

attributed it to Cr–O stretching vibrations, but that band did not appear in the bentorite spectrum.

X-ray powder diffraction experiment

A bentorite grain with weak extinction in the polarised light was selected and studied specially to check its suitability for single-crystal studies. Bentorite turned out to be a fine aggregate of disordered particles which produce Debye rings in the obtained 2D frame (Fig. 7) while weak single-crystal reflections belong to associated minor phases. The polycrystalline bentorite sample was analysed by X-ray powder diffraction.

High-accuracy synchrotron low-temperature measurements of the bentorite sample were performed at 100 and 250 K on a high-resolution powder diffraction beamline ID22 at the European Synchrotron Radiation Facility (ESRF, Grenoble, France). Diffraction data were collected at a low temperature to avoid heating-related dehydration under the strong X-ray beam. Powdered silicon ($a = 5.43119460 \text{ \AA}$) was used as a standard for the goniometer calibration and the X-ray wavelength refinement ($\lambda = 0.39996(4) \text{ \AA}$). The powdered bentorite sample was loaded into a 1-mm diameter thin-walled borosilicate glass capillary which was rotated at 1200 revolutions per minute for better count statistics. The X-ray diffraction data were collected in a range of $2\text{--}30^\circ 2\theta$, at a step of 0.002° .

The room-temperature (295 K) XRPD data were collected on a *Stoe STADI MP* X-ray powder diffractometer (CuK α 1 radiation, Ge(111) monochromator) at 2θ angles from 2 to 60° at a step of 0.015° , using powdered silicon as an external standard. The mineral phases coexisting with bentorite in the sample were identified with reference to the *PDF-4 Minerals* database (The Powder Diffraction File PDF-4+ 2009).

The XRPD patterns were analysed by the Rietveld method as implemented in the GSAS software suite of programmes (Larson and Von Dreele 2004) featuring the graphical interface EXPGUI (Toby 2001). Fitting was performed using Chebyshev polynomials for the background and a modified pseudo-Voigt function corrected for asymmetry for the diffraction profiles.

The structural data are deposited as CIF at the CCDC (CSD-1889236).

Re-examination of Cr³⁺-rich ettringite symmetry

The (SO₄)-groups in the structure of non-centrosymmetric Cr³⁺-bearing ettringite (space group $P31c$) are partly disordered (Seryotkin et al. 2018): split (SO₄)-groups at the S2 sites are oriented at 180° to one another (Fig. 5d) and show a ratio of 0.8/0.2. On the other hand, similar statistical orientation (Fig. 5b) should also occur for the centrosymmetric space group $P\bar{3}1c$ (Moore and Taylor 1970). To clear up the

situation, the structure of Cr-rich ettringite was additionally determined and refined (#1, Seryotkin et al. 2018) in the space group $P\bar{3}1c$ with reference to previously obtained single-crystal X-ray diffraction data.

The centrosymmetric solution yielded unrealistically short distances (≈ 2 Å) between oxygen atoms of the neighbour (SO₄)-groups. Refinement of some positions in anisotropic description was impossible, and some atomic sites tended to be split. Furthermore, the R-factor values in the centrosymmetric case were too high (R1 = 0.11, wR2 = 0.26). Therefore, the centrosymmetric space group $P\bar{3}1c$ is a wrong choice, and the disordering of (SO₄)-groups must have other causes. The lack of symmetry centre in the structure of Cr³⁺-bearing ettringite is also evident in the hemimorphism of its crystals.

Crystal structure of bentorite

Powder X-ray diffraction data for the bentorite sample are listed in the Table 2. All diffraction peaks ≥ 1 (on a 100-grade scale) either fit the standard ettringite unit cell or belong to minor ($\sim 1\%$) portlandite Ca(OH)₂ (PDF card 01-073-6988). Some smaller peaks (< 1) are produced by other minor ($< 1\%$) phases: gypsum (CaSO₄·2H₂O; PDF card 04-010-9409), fluorapatite (Ca₅(PO₄)₃F; PDF card 04-008-0676), and afwillite (Ca₃Si₂O₄(OH)₆; PDF card 04-011-6969) (Table 2), while the remaining peaks (Table 2) misfit the super-cell suggested by Gross (1980). The obtained diffraction data disagree with the inference of Gross (1980) that the *a*-parameter of the bentorite unit cell would be twofold relative to the ettringite metrics. No other version of distorted hexagonal cell worked to describe the remaining peaks, which must belong to some unidentified phases present in the sample. Temperature increase does not change much the X-ray diffraction patterns, except for shifting the peaks toward smaller angles as a result of thermal expansion. The trigonal unit cell of bentorite has the following parameters:

$$100 \text{ K: } a = 11.16150(5), c = 21.63017(19) \text{ \AA}, \\ V = 2333.650(19) \text{ \AA}^3;$$

$$250 \text{ K: } a = 11.17790(5), c = 21.7375(2) \text{ \AA}, V = 2352.12(2) \text{ \AA}^3;$$

$$295 \text{ K: } a = 11.2110(2), c = 21.7654(7) \text{ \AA}, V = 2369.10(7) \text{ \AA}^3.$$

The bentorite structure at 100 K was refined in the standard ettringite setting, using the structure of Cr³⁺-bearing ettringite (Seryotkin et al. 2018) as a starting model. The presence of portlandite was taken into account while other minor phases were neglected. The Cr³⁺ and Al occupancies of octahedral sites were refined with regard

to complete population. Both positions were found to be fully occupied by Cr atoms, and their occupancies were constrained to Cr_{1,0} in the final refinement. The occupancies of H₂O and OH-group sites were also refined at the first stage. The refinement showed full occupancies which were assumed fixed in the final refinement. The degree of orientation disordering of (SO₄)-groups was estimated at the initial step, as in the case of Cr³⁺-bearing ettringite (Seryotkin et al. 2018). The occupancy of alternative O sites tended to zero, and the final refinement was performed with ordered anion groups. Isotropic displacement parameters were refined for all non-H atoms. For H positions, the displacement parameters were fixed at 0.05. During the refinement, the O–H bond lengths of water molecules and (OH)-groups were restrained to 1.00(2) Å, and those of H–H were restrained to 1.67(1) Å. See Table 3 for experimental details of data collection and structure determination and *Supplementary materials* (CIF file, Tables S1 and S2) for the refinement results. Figures 8 and 9 show, respectively, the experimental and calculated profiles after structure refinement at 100 K and the resulting structure of bentorite.

The crystal-chemical formula of the ettringite–bentorite solid solution series is Ca₆^[81]M₂^[61]R₄(O, OH)₁₂·24H₂O, where M = Al, Si, and Cr³⁺; R = SO₄, CO₃, and H₂O. The M sites occupied by small trivalent cations are coordinated by six (OH)-groups which form regular octahedra. A medium-sized Ca²⁺ cation is surrounded by four (OH)-groups from around two neighbour M sites and four H₂O molecules; their coordination polyhedra may be described as double-capped trigonal prisms. Three neighbour columns built by M octahedra and Ca polyhedra aligned with the *c*-axis have hydrogen bonds with anion groups (SO₄)²⁻, (CO₃)²⁻ and also with H₂O at R sites between the columns (Fig. 8). The R occupancy by anion groups depends on M occupancy, namely the presence of Si⁴⁺ requires compensation of excess positive charge, and the number of anion groups at R sites will increase correspondingly. Vice versa, Si⁴⁺ atoms are expected to occupy M sites if the total number of anion groups exceeds 3 pfu. According to SEM EDS and EMPA, bentorite contains a vanishing amount of Si (Table 1), while both Raman and FTIR spectra show (CO₃)-groups as a vanishing impurity (Figs. 4, 6). Thus, anion groups in the analysed bentorite sample are limited to (SO₄)²⁻, which are distributed among three standard R positions. The fourth R site is occupied by H₂O molecules statistically distributed between O19 and O19'. Note again that all anion groups in the bentorite structure are ordered (Fig. 6b), unlike Cr³⁺-bearing ettringite with disordered (SO₄)-groups (Seryotkin et al. 2018). In principle, ordering of (SO₄)-groups in the bentorite structure may be due to conditions of low-temperature experiment, but they may become disordered at room temperature. On

Table 2 Powder X-ray diffraction data of bentorite sample

d_{obs} (Å)	I_{obs}	d_{calc} (Å) ^a	I_{calc}	hkl
10.8205	2.24	10.8151	1.95	002
9.6702	100.00	9.6661	100.00	010
8.8279	6.57	8.8250	4.90	011
8.1099	0.12			Fluorapatite
7.5667	0.19			Gypsum
7.2090	1.26	7.2071	1.16	012
6.5326	0.27			Afwillite
5.7816	1.96	5.7794	1.94	013
5.5826	36.51	5.5808	46.01	– 120
5.4086	0.31	5.4075	0.60	004
5.2517	0.07			Fluorapatite
5.0537	0.35			Afwillite
4.9608	7.66	4.9594	9.22	– 122, 112
4.8964	0.87			Portlandite
4.8344	0.31	4.8331	0.17	020
4.7209	6.93	4.7181	10.57	014, 021
4.4139	0.21	4.4125	0.35	022
4.2699	0.18			
4.1320	0.04			
4.0555	0.08			
4.0160	3.12	4.0146	3.45	023
3.9506	0.46	3.9486	0.42	015
3.8851	25.06	3.8835	42.67	–124, 114
3.7313	0.04			
3.6550	0.26	3.6535	0.19	– 130
3.6049	8.23	3.6035	12.07	024
3.4624	8.32	3.4613	12.67	– 132, 122
3.3801	0.12	3.3778	0.18	016
3.2598	1.86	3.2589	3.40	– 133, 123
3.2233	6.34	3.2220	10.42	030
3.1879	0.23	3.1869	0.32	031
3.1684	0.82			Afwillite
3.1089	0.41			Portlandite
3.0891	0.30	3.0879	0.65	032
3.0659	0.12			
3.0532	0.13			Afwillite
3.0440	0.16			Gypsum
3.0293	2.48	3.0282	3.33	– 126, 116
2.8643	0.05			
2.8302	0.99			Afwillite
2.8134	0.44			Afwillite
2.8012	0.99			Fluorapatite
2.7917	0.99	2.7909	1.27	– 135, 125, – 240
2.7690	14.80	2.7679	25.64	034
2.7208	0.78			Afwillite
2.7038	3.03	2.7029	6.34	008, 222
2.6825	0.39	2.6809	0.56	– 140
2.6616	0.70	2.6605	0.92	– 141
2.6254	1.75			Portlandite
2.6032	3.95	2.6021	8.14	– 142, 132
2.5671	12.09	2.5661	25.17	– 136, 126

Table 2 (continued)

d_{obs} (Å)	I_{obs}	d_{calc} (Å) ^a	I_{calc}	hkl
2.5138	0.92	2.5128	1.81	– 143, 133
2.4806	1.61	2.4797	3.92	– 244, 224
2.4347	1.06	2.4332	3.25	– 128, 118
2.4028	4.31	2.4019	9.33	– 144, 134
2.3606	0.48	2.3594	1.12	028, 127
2.3403	0.17	2.3323	0.31	019
2.3062	0.07			Afwillite
2.2909	0.11	2.2913	0.27	043
2.2796	0.13	2.2788	0.14	– 145
2.2498	0.28			Gypsum
2.2183	1.10	2.2176	1.70	– 250
2.2075	10.59	2.2066	21.02	– 246, 226
2.1734	1.81	2.1724	2.59	– 252, 232
2.1521	5.25	2.1513	11.40	– 146, 136
2.1203	0.85	2.1196	1.67	233
2.1103	1.80	2.1093	3.58	– 150
2.1005	0.24	2.0994	0.16	141
2.0711	0.56	2.0703	1.09	– 152
2.0525	2.10	2.0517	4.35	– 254, 234
2.0255	0.16	2.0248	0.23	137, 143
2.0178	0.42	2.0168	1.05	– 1.2.10, 1.1.10
2.0094	0.23	2.0079	0.25	– 139
1.9816	0.10			Gypsum
1.9742	0.33	1.9734	0.53	– 255, 235
1.9659	0.25	1.9651	0.51	– 154, 144
1.9424	0.90	1.9417	1.76	– 248, 228
1.9340	3.01	1.9332	6.78	050
1.9238	0.48	1.9267	0.45	0.1.11, 039
1.9046	1.11	1.9037	2.87	– 148, 138, 047
1.8971	0.32	1.8960	0.30	– 155
1.8899	0.14	1.8888	0.36	– 256, 236
1.8839	0.18			
1.8619	2.31	1.8610	6.29	– 1.3.10, 1.2.10, – 360
1.8384	0.50			
1.8341	1.25	1.8333	2.83	– 362, 332
1.8212	0.65	1.8203	1.25	054, – 261
1.8024	2.03	1.8018	4.08	0.0.12, 048, – 262
1.7963	0.67	1.7959	0.06	0.3.10
1.7948	0.69			Portlandite
1.7729	0.40	1.7720	1.34	0.1.12
1.7709	0.38	1.7708	0.16	– 263, 243
1.7598	1.49	1.7591	3.48	– 364, 334
1.7477	0.24	1.7421	0.02	– 157, 147
1.7368	0.62	1.7361	1.64	– 160
1.7316	0.26	1.7310	0.30	1.2.11, – 264
1.7158	1.73	1.7153	3.98	– 1.2.12, 1.1.12
1.6988	0.14			Afwillite
1.6890	0.48	1.6883	0.77	0.2.12, 153
1.6845	1.82	1.6834	3.59	– 1.4.10, 1.3.10
1.6638	3.24	1.6831	8.54	– 158, 148
1.6537	0.47	1.6530	0.87	– 164, 154

Table 2 (continued)

d_{obs} (Å)	I_{obs}	d_{calc} (Å) ^a	I_{calc}	hkl
1.6118	2.17	1.6110	4.89	060
1.5982	0.12			Gypsum
1.5897	0.24	1.5891	0.55	– 370
1.5862	0.22	1.5856	0.18	– 1.4.11, 1.3.11
1.5733	2.39	1.5726	5.46	0.3.12, 058
1.5523	0.23	1.5722	1.33	– 372, 342
1.5485	0.31	1.5478	0.57	– 270
1.5452	0.23	1.5440	0.42	064
1.5332	0.25	1.5322	0.59	– 272, 252
1.5253	0.32	1.5246	0.81	– 374, 344
1.5146	1.87	1.5139	5.40	– 2.4.12, 2.2.12, – 268, 248
1.4967	0.44	1.4958	1.31	– 1.4.12, 1.3.12
1.4888	0.86	1.4881	1.94	– 274, 254
1.4820	0.21			Portlandite
1.4747	0.17	1.4741	0.37	– 1.7.0
1.4721	0.17	1.4713	0.19	2.3.11
1.4680	0.17			
1.4615	0.45	1.4609	1.41	– 168, 158
1.4547	0.53	1.4541	0.99	– 376, 346
1.4461	0.22			Portlandite
1.4446	0.14	1.4442	0.18	– 173, 163
1.4229	0.44	1.4225	0.97	– 1.3.14, 1.2.14, – 276, 256, – 174, 164
1.4112	0.18	1.4104	0.45	– 3.6.10, 3.3.10
1.3994	0.32	1.3987	1.07	– 2.5.12, 2.3.12
1.3843	0.20	1.3840	0.41	068
1.3786	0.14	1.3781	0.15	– 381
1.3712	0.23	1.3703	0.64	– 1.5.12, 1.4.12
1.3517	0.79	1.3519	1.06	0.0.16
1.3438	0.29	1.3509	0.76	– 484
1.3406	0.52	1.3405	0.01	– 280
1.3394	0.60	1.3389	1.36	0.1.16
1.3308	0.46	1.3303	0.99	– 282, 262
1.3188	0.37	1.3184	0.68	0.5.12
1.3154	0.33	1.3139	0.83	– 1.2.16, 1.1.16
1.3017	0.95	1.3011	1.97	– 486, 446, – 284, 264
1.2951	0.18	1.2945	0.61	– 3.6.12, 3.3.12
1.2810	0.34	1.2805	0.89	– 3.7.10, – 180
1.2719	0.48	1.2714	1.02	– 182, 172
1.2687	0.25	1.2677	0.49	– 2.5.14, 2.3.14
1.2572	0.15	1.2564	0.21	– 286, 266
1.2511	0.14	1.2504	0.37	– 1.6.12, 1.5.12
1.2465	0.67	1.2459	1.59	– 184, 174
1.2397	0.18	1.2398	0.27	– 488, 448
1.2183	0.63	1.2178	1.25	– 390
1.2104	0.28	1.2102	0.35	– 392
1.1923	0.30	1.1920	0.55	– 3.7.12, 3.4.12
1.1886	0.54	1.1881	1.09	– 394, 364
1.1803	0.27	1.1797	0.53	– 2.6.14, 2.4.14
1.1748	0.71	1.1743	1.29	– 2.7.12, 2.5.12
1.1546	0.26	1.1539	0.47	1.5.14, – 294, 274

Table 2 (continued)

d_{obs} (Å)	I_{obs}	d_{calc} (Å) ^a	I_{calc}	hkl
1.1423	0.29	1.1415	0.52	– 1.3.18, 1.2.18
1.1391	0.65	1.1382	1.34	– 1.5.16, 1.4.16
1.1256	0.27	1.1253	0.42	– 498, 458, 182
1.1226	0.28	1.1222	0.62	– 296, 276
1.1165	0.13	1.1162	0.30	– 5.10.0
1.1084	0.55	1.1078	1.07	0.5.16, – 3.7.14, 3.4.14
1.1036	0.62	1.1033	0.81	– 4.8.12, 4.4.12

^aIn the case of several overlapped reflections, average values are quoted

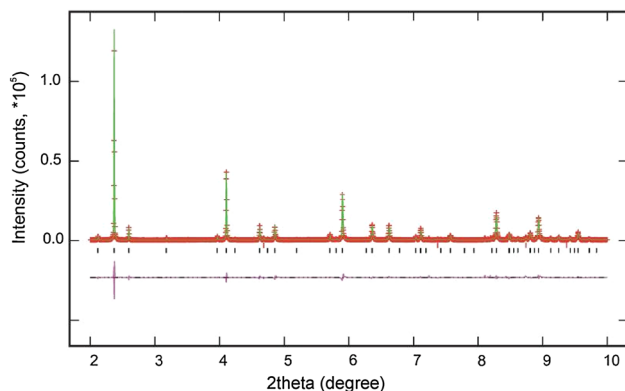


Fig. 8 Rietveld refinement of bentorite structure at 100 K, observed (+ symbols) and calculated (solid line) profiles. Tick marks are Bragg peaks. Difference (observed minus calculated) curve is plotted at the bottom

Table 3 Basic crystallographic and experimental data for bentorite at 100 K

a (Å)	11.16150(5)
c (Å)	21.63017(19)
V (Å ³)	2333.650(19)
Space group	$P31c$
X-ray wavelength	0.39996(4) Å
2θ range (°)	2–30
Step	0.002
Nobs	13,999
Number of variables	155
R_p	0.0888
R_{wp}	0.1184
R_{F2} for 2084 reflections	0.0655
GOF	3.33
χ^2 for 155 variables	11.12

the other hand, Al-free bentorite and Cr-free ettringite differ only in the type of atoms that occupy the M sites (Cr^{3+} instead of Al^{3+}). Given that all anion groups in the structure of Cr-free ettringite are ordered (Moore and Taylor

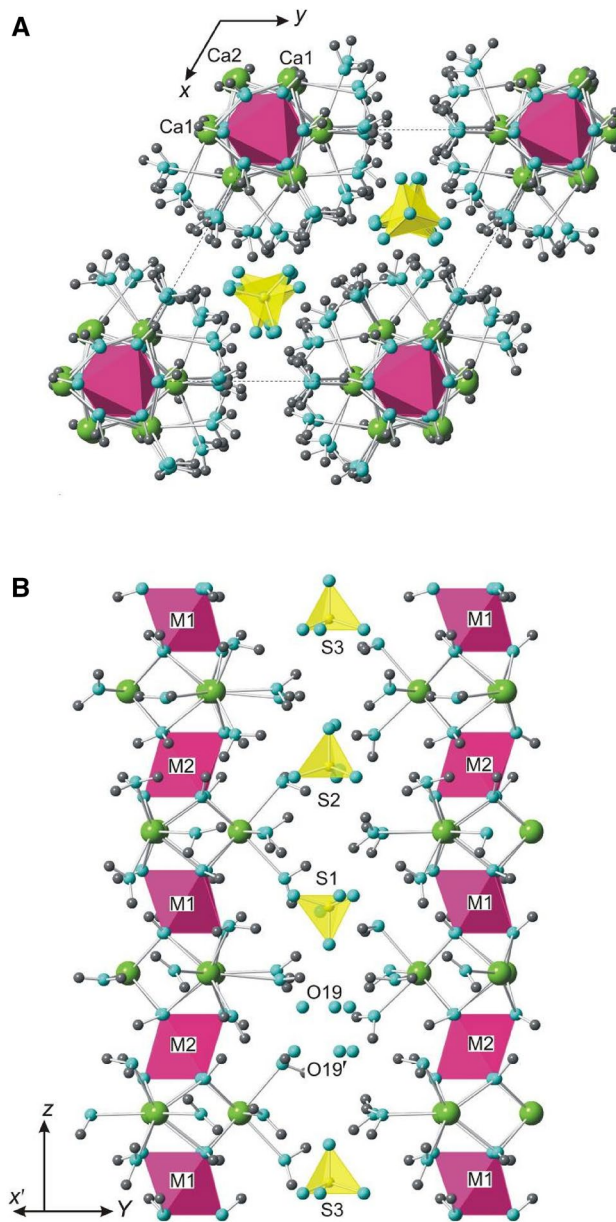


Fig. 9 Crystal structure of bentorite, projected on z -axis (a) and (011) plane (b). The refined structure of bentorite suggests a formula of $\text{Ca}_6(\text{Cr}_{2.00}^{3+})^M [(\text{SO}_4)_{3.00} \text{H}_2\text{O}]_{\Sigma 4.00}^R (\text{OH})_{12} (\text{H}_2\text{O})_{24}$

1970; Hartman and Berliner 2006; Seryotkin et al. 2018), the disordering of the anion groups may be, to a high probability, due to statistical occupancies of M sites by Al and Cr³⁺ cations, and is likely common to the intermediate members of the ettringite–bentorite series.

The average Cr–O distance in the structure (1.97 Å) approaches the sum of effective ion radii of [6]Cr³⁺ and (4)O²⁻ (Shannon 1976), with regard to their coordination. These distances in Ca1 and Ca2 polyhedra are similar: 2.47 Å for Ca1–O and 2.49 Å for Ca2–O.

The distances and angles associated with hydrogen bonds, as well as the H···O distances in the ettringite structure according to powder neutron diffractometry (Hartman and Berliner 2006), are listed in Table 4. The system of hydrogen bonds in bentorite is obviously similar to that in the ettringite structure.

Table 5 shows calculated bond strengths (Brese and O’Keeffe 1991) for Ca, Cr, and S positions in the bentorite structure. The bond valence sum for Ca positions slightly exceeds the formal valence of the Ca²⁺ cation, and the same is valid for other positions, except for S1. This difference may be partly due to structure compression by cooling. The interatomic distances in the bentorite structure are ≈0.5% shorter at 100 K than at ambient conditions. This correction makes the bond valence sum notably closer to the formal cation valence. On the other hand, the bond valence sum variations within ±0.1 are quite acceptable, judging by published data on the structure of ettringite group compounds (Seryotkin et al. 2018). The previously discovered tendency

Table 5 Bond-strength calculation for bentorite

Ca1–O1	0.23	Ca2–O2	0.29
Ca1–O1	0.40	Ca2–O2	0.23
Ca1–O3	0.21	Ca2–O4	0.31
Ca1–O3	0.33	Ca2–O4	0.36
Ca1–Ow6	0.26	Ca2–Ow5	0.22
Ca1–Ow8	0.36	Ca2–Ow7	0.29
Ca1–Ow10	0.34	Ca2–Ow9	0.13
Ca1–Ow12	0.09	Ca2–Ow11	0.20
Σ	2.21	Σ	2.03
M1–O1(3×)	0.59	M2–O3(3×)	0.57
M1–O2(3×)	0.47	M2–O4(3×)	0.45
Σ	3.19	Σ	3.07
S1–O13	1.56	S2–O14	1.74
S1–O16(3×)	1.48	S2–O17(3×)	1.51
Σ	5.99	Σ	6.26
S3–O15	1.99		
S3–O18(3×)	1.40		
Σ	6.18		

of increasing difference in average Ca–O distances between the Ca1 and Ca2 positions with increasing Cr³⁺ content does not work in the case of bentorite in which the average Ca1–O and Ca2–O distances are similar.

As reported earlier (Seryotkin et al. 2018), the symmetry of ettringite group minerals is controlled by the R occupancy of the anion groups (SO₄)²⁻, (CO₃)²⁻, and [B(OH)₄]⁻.

Table 4 Hydrogen bonds in the bentorite structure in comparison with neutron diffraction data (Hartman and Berliner 2006) (right column)

O–H···O	O–H (Å)	H···O (Å)	O···O (Å)	∠O–H···O (°)	H···O (Å)
O1–H1···Ow5	1.11(2)	2.28(19)	3.25(3)	146.4	2.340
O2–H2···Ow6	1.064(17)	2.28(17)	2.93(3)	117.9	2.235
O3–H3···Ow7	1.022(14)	2.15(16)	3.05(4)	145.6	2.347
O4–H4···Ow8	1.091(12)	2.24(19)	3.23(3)	145.1	2.130
Ow5–H5A···O18	1.028(11)	2.03(7)	2.66(2)	116.7	1.824
Ow5–H5B···O16	1.09(3)	2.15(16)	2.85(3)	119.6	1.894
Ow6–H6A···O18	1.01(2)	2.12(15)	2.92(3)	135.1	1.769
Ow6–H6B···O16	1.010(16)	1.95(6)	2.77(2)	138.0	1.813
Ow7–H7A···O19′	1.16(4)	2.06(12)	2.85(2)	122.4	2.218
Ow7–H7B···O17	1.03(2)	2.05(6)	2.79(2)	126.5	2.019
Ow8–H8A···O19′	1.003(7)	2.01(6)	2.79(3)	133.7	1.752
Ow8–H8B···O17	1.006(11)	2.02(6)	2.82(2)	134.7	2.025
Ow9–H9A···O17	1.014(11)	1.97(7)	2.60(2)	117.8	1.708
Ow9–H9B···O16	1.012(11)	2.03(7)	2.69(2)	120.8	1.764
Ow10–H10A···O14	1.02(2)	2.05(6)	2.982(18)	150.9	1.890
Ow10–H10B···O18	1.001(7)	2.03(6)	2.74(2)	126.2	2.014
Ow11–H11A···Ow9	1.04(3)	2.24(14)	2.99(3)	127.2	1.863
Ow11–H11B···O15	1.010(7)	2.06(6)	2.916(17)	141.8	1.906
Ow12–H12A···Ow10	1.14(4)	2.15(9)	3.11(3)	139.1	2.078
Ow12–H12B···O13	1.002(7)	1.99(6)	2.86(3)	143.4	2.223

Eight out of ten ettringite group minerals have non-centrosymmetric structures according to orientation ordering of $(\text{SO}_4)^{2-}$ and/or $[\text{B}(\text{OH})_4]^-$ tetrahedral groups (Pekov et al. 2012). The centrosymmetric structures of carraraite, space group $P6_3/m$ (Merlino and Orlandi 2001), and kottenheimite, space group $P6_3/m$ (Chukanov et al. 2012), have four anion groups per formula unit, i.e., the R occupancy is complete.

However, the complete R occupancy by itself cannot ensure the centrosymmetric structure: thaumasite (Gatta et al. 2012), imayoshiite (Nishio-Hamane et al. 2015), hielscherite (Pekov et al. 2012), and jourvaskite (Granger and Protas 1969; Chukanov et al. 2018) likewise have four anion groups pfu, but their space group is $P6_3$. Both bentorite and ettringite have three anion groups pfu, while only $(\text{SO}_4)^{2-}$ groups are present in all analysed bentorite samples (Gross 1980; Sokol et al. 2011). Therefore, Cr^{3+} substitution for Al is the only difference between the bentorite and ettringite compositions, i.e., they are isostructural.

The X-ray powder data reported by Gross (1980) provide a poor description for the claimed super-cell with an a -parameter twice the size of the ettringite unit cell. Three reflections out of those listed by Gross (1980, Table 2) were identified as super-structures (with odd h and/or k). The unit cell sizes refined in a standard ettringite setting differ from the values of Gross (1980): $a = 11.185$, $c = 21.23$ Å vs $a/2 = 11.175$, $c = 2.41$ Å. The super-structure peak with $d_{\text{meas.}} = 2.61$ Å can be indexed as hkl 132 in the ettringite setting; another reflection with $d_{\text{meas.}} = 6.11$ Å has the indices hkl of a super-cell (212 and 301 according to Gross (1980)), while the calculations of d_{212} and d_{301} give the values 6.03 Å and 6.18 Å, respectively. Only one reflection suggested by Gross (1980) ($d_{\text{meas.}} = 4.29$ Å) has consistent indexing: $d_{214} = 4.30$ Å and $d_{313} = 4.28$ Å. The diffraction profile we collected misses the $d = 6.11$ Å peak, while that of $d = 4.2699$ Å comparable in its position with the $d_{\text{meas.}} = 4.29$ Å peak has a much lower intensity (0.18 against 3). Furthermore, the difference between the calculated d_{214} and d_{313} values of our bentorite super-cell (4.347 and 4.303 Å, respectively) and the observed peak position is at least 0.3 Å, i.e., much greater than the acceptable misfit of $\sim 10^{-3}$ Å (Table 2). Therefore, the unidentified super-structure peaks most likely belong to minor phases.

Conclusions

High-accuracy synchrotron low-temperature measurements coupled with high-resolution powder diffraction of natural bentorite from its holotype locality (the Hatrum Basin, Negev Desert) were performed at 100, 250 K and 295 K. According to structure refinement, the crystal chemical formula of the studied sample may be presented as $\text{Ca}_6\text{Cr}_2^{\text{M}}[\text{SO}_4]_3^{\text{R}}(\text{OH})_{12} \cdot 26\text{H}_2\text{O}$. Chemical analyses

of natural bentorite ($\text{Ca}_6(\text{Cr}_{1.88}\text{Al}_{0.06}\text{Si}_{0.05}\text{Fe}_{0.02}\text{Mn}_{0.01})_{\Sigma 2.02}(\text{SO}_4)_{3.02}(\text{OH})_{12} \cdot 26\text{H}_2\text{O}$) support its similarity to the Cr^{3+} -rich end member of the ettringite–bentorite series. The results show that bentorite is isostructural with ettringite, space group $P31c$, which confirms the existence of the ettringite $\text{Ca}_6\text{Al}_2^{\text{M}}[\text{SO}_4]_3^{\text{R}}(\text{OH})_{12} \cdot 26\text{H}_2\text{O}$ –bentorite $\text{Ca}_6\text{Cr}_2^{\text{M}}[\text{SO}_4]_3^{\text{R}}(\text{OH})_{12} \cdot 26\text{H}_2\text{O}$ solid solution series over the whole range of compositions $0 \leq \text{Cr}^{3+}/(\text{Al} + \text{Cr}^{3+}) \leq 1$. Our data, obtained with more advanced analytical facilities, allow updates to previous inferences by Gross (1980) concerning the bentorite metrics, namely she misidentified the weak peaks, which actually belong to minor phases, as super-structures responsible for twofold unit cell size of bentorite relative to ettringite, and assigned the space group $P6_3/mmc$ to bentorite based on wrong earlier X-ray powder diffraction data for ettringite (Bannister et al. 1936).

The Raman spectrum of bentorite collected for the first time shows a set of characteristic bands (540, 620, 1000, 1140 cm^{-1}) different from those in ettringite and in its Cr^{3+} -rich variety. This difference may be used as a guide in preliminary identification and become a valuable tool for discrimination between Cr^{3+} -rich ettringite and bentorite, which is otherwise problematic. The reason is that dehydration in vacuum causes cracking of crystals and make ettringite and/or bentorite unfit for XRD analyses after SEM or microprobe examination (Gross 1980; Thiery et al. 2017; Seryotkin et al. 2018).

Proceeding from our own results and published experimental evidence (Wieczorek-Ciurowa et al. 2001; Cody et al. 2004), we may infer, to a high probability, that the presence of abundant Cr^{3+} required for crystallisation of bentorite from an alkaline aqueous solution leads to dramatic changes to the crystal habit. The Cr^{3+} ion that adsorbs only on the rectangular prism faces retards their growth but stimulates rapid growth of termination faces. As a result, bentorite commonly occurs as fibrous aggregates or clots, while its single crystals suitable for XRD examination are exceptionally rare.

We have found out for the first time that Cr^{3+} -rich ettringite and bentorite can be identified according to their Raman spectra which have some distinctive features. The spectra of Cr^{3+} -rich ettringite and bentorite differ from that of ettringite at these bandwidths in notably greater intensities of the ~ 450 , ~ 550 , and ~ 620 cm^{-1} bands and in the presence of a prominent band at ~ 850 cm^{-1} . The difference is mostly in relative intensities of the 540–550- cm^{-1} band, which is the strongest in bentorite. These features of Raman spectra allow nondestructive selection of crystals, which have the highest contents of Cr and are potentially suitable for the X-ray diffraction analysis. The SEM-based selection of crystals for further structural

studies is inapplicable because ettringite is prone to dehydration in vacuum.

Acknowledgements The study was supported by the Russian Science Foundation, Grant 17-17-01056. The European Synchrotron Radiation Facility is acknowledged for the allocation of experimental beam time. The authors are indebted to Boris Zakharov and to Wilson Mogodi for technical support during the LT experiments.

References

- Bannister FA, Hey MH, Bernal JD (1936) Ettringite from Scawt Hill Co. Antrim. *Mineral Mag* 24:324–329. <https://doi.org/10.1180/minmag.1936.024.153.05>
- Beattie JK, Best SP (1997) Structures and spectroscopy of hexaaquametal(III) ions. *Coord Chem Rev* 166:391–415. [https://doi.org/10.1016/S0010-8545\(97\)00049-0](https://doi.org/10.1016/S0010-8545(97)00049-0)
- Bentor YK, Gross S, Heller L (1963) High-temperature minerals in non-metamorphosed sediments in Israel. *Nature* 199:478–479. <https://doi.org/10.1038/199478a0>
- Brese NE, O’Keeffe M (1991) Bond-valence parameters for solids. *Acta Crystallogr B* 47:192–197. <https://doi.org/10.1107/S0108768190011041>
- Brough AR, Atkinson A (2001) Micro-Raman spectroscopy of thaumasite. *Cem Concr Res* 31:421–424. [https://doi.org/10.1016/S0008-8846\(00\)00459-2](https://doi.org/10.1016/S0008-8846(00)00459-2)
- Burg A, Starinsky A, Bartov Y, Kolodny Y (1991) Geology of the Hatrurim Formation (“Mottled Zone”) in the Hatrurim basin. *Isr J Earth Sci* 40:107–124
- Burg A, Kolodny Y, Lyakhovsky V (1999) Hatrurim-2000: the “Mottled Zone” revisited, forty years later. *Isr J Earth Sci* 48:209–223
- Chukanov NV (2014) Infrared spectra of mineral species. Springer, Dordrecht Heidelberg New York London. <https://doi.org/10.1007/978-94-007-7128-4>
- Chukanov NV, Britvin SN, Van KV, Möckel S, Zadov AE (2012) Kottenheimite, $\text{Ca}_3\text{Si}(\text{OH})_6(\text{SO}_4)_2 \cdot 12\text{H}_2\text{O}$, a new member of the ettringite group from the Eifel area, Germany. *Can Mineral* 50:55–63. <https://doi.org/10.3749/canmin.50.1.55>
- Chukanov NV, Zubkova NV, Pautov LA, Göttlicher J, Kasatkin AV, Van KV, Ksenofontov DA, Pekov IV, Vozchikova SA, Pushcharovsky DYu (2018) Jouravskite: refined data on the crystal structure, chemical composition and spectroscopic properties. *Phys Chem Minerals*. <https://doi.org/10.1007/s00269-018-1012-8> (in press)
- Cody AM, Lee H, Cody RD, Spry PG (2004) The effect of chemical environment on the nucleation, growth, and stability of ettringite $[\text{Ca}_3\text{Al}(\text{OH})_6]_2(\text{SO}_4)_3 \cdot 26\text{H}_2\text{O}$. *Cem Concr Res* 34:869–881. <https://doi.org/10.1016/j.cemconres.2003.10.023>
- Deb S, Manghnani M, Ross K, Livingston R, Monteiro P (2003) Raman scattering and X-ray diffraction study of the thermal decomposition of an ettringite-group crystal. *Phys Chem Minerals* 30:31–38. <https://doi.org/10.1007/s00269-002-0279-x>
- Deer WA, Howie RA, Zussman J (1986) Rock-forming minerals, V. 1B: disilicates and ring silicates. Geological Society, London
- Drebushchak VA, Seryotkin YuV, Kokh SN, Sokol EV (2013) Natural specimen of triple solid state solution ettringite–thaumasite–chromate–ettringite. *J Therm Anal Calorim* 114:777–783. <https://doi.org/10.1007/s10973-013-2989-3>
- Elie M, Techer I, Trotignon L, Khoury H, Salameh E, Vandamme D, Boulvais P, Fourcade S (2007) Cementation of kerogen-rich marls by alkaline fluids released during weathering of thermally metamorphosed marly sediments. Part II: Organic matter evolution, magnetic susceptibility and metals (Ti, Cr, Fe) at the Khushaym Matruck natural analogue (central Jordan). *Appl Geochem* 22:1311–1328. <https://doi.org/10.1016/j.apgeochem.2007.02.013>
- Fleurance S, Cuney M, Malartre M, Reyx J (2013) Origin of the extreme polymetallic enrichment (Cd, Cr, Mo, Ni, U, V, Zn) of the Late Cretaceous–Early Tertiary Belqa Group, central Jordan. *Palaeogeogr Palaeoclimatol Palaeoecol* 369:201–219. <https://doi.org/10.1016/j.palaeo.2012.10.020>
- Frost RL (2004) Raman microscopy of selected chromate minerals. *J Raman Spectr* 35:153–158. <https://doi.org/10.1002/jrs.1121>
- Frost R, Lopez A, Xi Y, Scholz R, Magela da Costa G, Lima RMF, Granja A (2013) The spectroscopic characterization of the sulphate mineral ettringite from Kuruman manganese deposits, South Africa. *Vib Spectrosc* 68:266–271. <https://doi.org/10.1016/j.vibspec.2013.08.011>
- Gatta GD, McIntyre GJ, Swanson JG, Jacobsen SD (2012) Minerals in cement chemistry: a single-crystal neutron diffraction and Raman spectroscopic study of thaumasite, $\text{Ca}_3\text{Si}(\text{OH})_6(\text{CO}_3)(\text{SO}_4) \cdot 12\text{H}_2\text{O}$. *Am Mineral* 97:1060–1069. <https://doi.org/10.2138/am.2012.4058>
- Gilat A (1998) Hydrothermal activity and hydro-explosions as a cause of natural combustion and pyrolysis of bituminous rocks: the case of Pliocene metamorphism in Israel (Hatrurim Formation), *Geol. Surv. Isr. Curr Res* 11:96–102
- Goetz-Neunhoeffler F, Neubauer J, Schwesig P (2006) Mineralogical characteristics of Ettringites synthesized from solutions and suspensions. *Cem Concr Res* 36:65–70. <https://doi.org/10.1016/j.cemconres.2004.04.037>
- Granger MM, Protas J (1969) Détermination et étude de la structure cristalline de la jouravskite $\text{Ca}_3\text{Mn}^{\text{IV}}(\text{SO}_4)(\text{CO}_3)(\text{OH})_6 \cdot 12\text{H}_2\text{O}$. *Acta Crystallogr B* 25:1943–1951
- Gross S (1977) The mineralogy of the Hatrurim formation, Israel. *Geol Surv Isr Bull* 70:80
- Gross S (1980) Bentorite. A new mineral from the Hatrurim area, west of the Dead Sea, Israel. *Isr J Earth Sci* 29:81–84
- Hartman MR, Berliner R (2006) Investigation of the structure of ettringite by time-of-flight neutron powder diffraction techniques. *Cem Concr Res* 36:364–370. <https://doi.org/10.1016/j.cemconres.2005.08.004>
- Hauff PL, Foord EE, Rosenblum S, Hakki W (1983) Hasheimite, $\text{Ba}(\text{Cr,S})\text{O}_4$, a new mineral from Jordan. *Am Mineral* 68:1223–1225
- Khoury HN, Al-Zoubi AS (2014) Origin and characteristics of Cr-smectite from Suweileh area. *Jordan Appl Clay Sci* 90:43–52. <https://doi.org/10.1016/j.clay.2014.01.00>
- Khoury H, Nassir S (1982) High temperature mineralization in Maqarin area, North Jordan. *Neues Jahrb. Mineralogie Abh* 144:197–213
- Khoury HN, Sokol EV, Kokh SN, Seryotkin YV, Nigmatulina EN, Goryainov SV, Belogub EV, Clark ID (2016) Tululite, $\text{Ca}_{14}(\text{Fe}^{3+}, \text{Al})(\text{Al}, \text{Zn}, \text{Fe}^{3+}, \text{Si}, \text{P}, \text{Mn}, \text{Mg})_{15}\text{O}_{36}$: a new Ca zincate-aluminate from combustion metamorphic marbles, central Jordan. *Mineral Petrol* 110:125–140. <https://doi.org/10.1007/s00710-015-0413-3>
- Kolodny Y, Gross S (1974) Thermal metamorphism by combustion of organic matter: isotopic and petrological evidence. *J Geol* 82:489–506
- Larson A, Von Dreele R (2004) General Structure Analysis System (GSAS), Los Alamos National Laboratory Report LAUR 86–748
- Liu C, Hystad G, Golden JJ, Hummer DR, Downs RT, Morrison ShM, Ralph JP, Hazen RM (2017) Chromium mineral ecology. *Am Mineral* 102:612–619. <https://doi.org/10.2138/am-2017-5900>
- Merlino S, Orlandi P (2001) Carraraite and zaccagnaite, two new minerals from the Carrara marble quarries: their chemical compositions, physical properties, and structural features. *Am Mineral* 86:1293–1301. <https://doi.org/10.2138/am-2001-1017>
- Model S506 Interactive Peak Fit (2002) User’s manual. Canberra Industries Inc, Canberra

- Moore A, Taylor HFW (1970) Crystal structure of ettringite. *Acta Crystallogr B* 26:386–393. <https://doi.org/10.1107/S0567740870002443>
- Möschner G, Lothenbach B, Winnefeld F, Ulrich A, Figi R, Kretzschmar R (2009) Solid solution between Al-ettringite and Fe-ettringite ($\text{Ca}_6[\text{Al}_{1-x}\text{Fe}_x(\text{OH})_6]_2(\text{SO}_4)_3 \cdot 26\text{H}_2\text{O}$). *Cem Concr Res* 39:482–489. <https://doi.org/10.1016/j.cemconres.2009.03.001>
- Myneni S, Traina S, Waychunas G, Logan T (1998) Vibrational spectroscopy of functional group chemistry and arsenate coordination in ettringite. *Geochim Cosmochim Acta* 62(21/22):3499–3514. [https://doi.org/10.1016/S0016-7037\(98\)00221-X](https://doi.org/10.1016/S0016-7037(98)00221-X)
- Nishio-Hamane D, Ohnishi M, Momma K, Shimobayashi N, Miyawaki R, Minakawa T, Inabaet S (2015) Imayoshiite, $\text{Ca}_3\text{Al}(\text{CO}_3)[\text{B}(\text{OH})_4(\text{OH})_6 \cdot 12\text{H}_2\text{O}]$, a new mineral of the ettringite group from Ise City, Mie Prefecture, Japan. *Mineral Mag* 79:413–423. <https://doi.org/10.1180/minmag.2015.079.2.18>
- Novikov I, Vapnik Y, Safonova I (2013) Mud volcano origin of the Mottled Zone, South Levant. *Geosci Front* 4:597–619. <https://doi.org/10.1016/j.gsf.2013.02.005>
- Ogawa K, Roy DM (1982) $\text{C}_4\text{A}_3\text{S}$ hydration, ettringite formation, and its expansion mechanism: III. Effect of CaO, NaOH and NaCl; conclusions. *Cem Concr Res* 12:247–256. [https://doi.org/10.1016/0008-8846\(82\)90011-4](https://doi.org/10.1016/0008-8846(82)90011-4)
- Pekov IV, Chukanov NV, Britvin SN, Kabalov YK, Göttlicher J, Yapaskurt VO, Zadov AE, Krivovichev SV, Shüller W, Ternes B (2012) The sulfite anion in ettringite-group minerals: a new mineral species hielscherite, $\text{Ca}_3\text{Si}(\text{OH})_6(\text{SO}_4)(\text{SO}_3) \cdot 11\text{H}_2\text{O}$, and the thaumasite–hielscherite solid-solution series. *Mineral Mag* 76:1133–1152. <https://doi.org/10.1180/minmag.2012.076.5.06>
- Perkins RB, Palmer CD (1999) Solubility of ettringite ($\text{Ca}_6[\text{Al}(\text{OH})_6]_2(\text{SO}_4)_3 \cdot 26\text{H}_2\text{O}$) at 5–75 °C. *Geochim Cosmochim Acta* 63:1969–1980. [https://doi.org/10.1016/S0016-7037\(99\)00078-2](https://doi.org/10.1016/S0016-7037(99)00078-2)
- Pheodorin MA, Bobrov VA, Chebykin EP, Goldberg EL, Melgunov MS, Filippova SV, Zolotarev KV (2000) Comparison of synchrotron radiation X-ray fluorescence with conventional techniques for the analysis of sedimentary samples. *J Geostand Geolanal* 24:205–216. <https://doi.org/10.1111/j.1751-908X.2000.tb00772.x>
- Pöllmann H, Kuzel H-J (1990) Solid solution of ettringites: Part I: Incorporation of OH^- and CO_3^{2-} in $3\text{CaO} \cdot \text{Al}_2\text{O}_3 \cdot 32\text{H}_2\text{O}$. *Cem Concr Res* 20:941–947
- Pöllmann H, Kuzel H-J, Wenda R (1989) Compounds with ettringite structure. *N Jb Mineral Abh* 160:133–158
- Pöllmann H, Auer S, Kuzel H-J (1993) Solid solution of ettringites: part II: incorporation of $\text{B}(\text{OH})_4^-$ and CrO_4^{2-} in $3\text{CaO} \cdot \text{Al}_2\text{O}_3 \cdot 3\text{CaSO}_4 \cdot 32\text{H}_2\text{O}$. *Cem Concr Res* 23:422–430
- Renaudin G, Segni R, Mentel D, Nedelec J-M, Leroux F, Taviot-Gueho C (2007) A Raman study of the sulfated cement hydrates: ettringite and monosulfoaluminate. *J Adv Concr Technol* 5(3):299–312. <https://doi.org/10.3151/jact.5.299>
- Seryotkin YuV, Sokol EV, Kokh SN, Murashko MN (2018) Natural Cr^{3+} -rich ettringite: occurrence, properties, and crystal structure. *Phys Chem Minerals* 45:279–292. <https://doi.org/10.1007/s00269-017-0917-y>
- Shannon RD (1976) Revised effective ionic radii and systematic studies of interatomic distances in halides and chalcogenides. *Acta Crystallogr A* 32:751–767
- Sharygin VV (2019) A hibonite-spinel-corundum-hematite assemblage in plagioclase-clinopyroxene pyrometamorphic rocks, Hatrurim Basin, Israel: mineral chemistry, genesis and formation temperatures. *Mineral Mag* 83(1):1–26. <https://doi.org/10.1180/mgm.2018.138>
- Sokol E, Novikov I, Zateeva S, Vapnik Y, Shagam R, Kozmenko O (2010) Combustion metamorphic rocks as indicators of fossil mud volcanism: new implications for the origin of the Mottled Zone, Dead Sea rift area. *Basin Res* 22:414–438. <https://doi.org/10.1111/j.1365-2117.2010.00462.x>
- Sokol EV, Gaskova OL, Kokh SN, Kozmenko OA, Seryotkin YuV, Ye V, Murashko MN (2011) Chromatite and its Cr^{3+} - and Cr^{6+} -bearing precursor minerals from the Nabi Musa Mottled Zone complex, Judean Desert. *Am Mineral* 96:659–674. <https://doi.org/10.2138/am.2011.3487>
- Sokol EV, Kokh SN, Vapnik Y, Thiéry V, Korzhova SA (2014) Natural analogues of belite sulfoaluminate cement clinkers from Negev desert, Israel. *Am Mineral* 99:1471–1487. <https://doi.org/10.2138/am.2014.4704>
- Terai T, Mikuni A, Komatsu R, Ikeda K (2006) Synthesis of Cr(VI)-ettringite in portlandite suspensions as a function of pH. *J Ceram Soc Jpn* 114:299–302. <https://doi.org/10.2109/jcersj.114.299>
- The Powder Diffraction File PDF-4+ (2009) International Centre for Diffraction Data, Release
- Thiéry V, Trincal V, Davy CA (2017) The elusive ettringite under the high-vacuum SEM—a reflection based on natural samples, the use of Monte Carlo modelling of EDS analyses and an extension to the ettringite group minerals. *J Microsc* 268(1):84–93. <https://doi.org/10.1111/jmi.12589>
- Toby BH (2001) EXPGUI, a graphical user interface for GSAS. *J Appl Crystallogr* 34:210–213. <https://doi.org/10.1107/S0021889801002242>
- Tregenna-Piggott PLW, Best SP (1996) Single-crystal Raman spectroscopy of the rubidium alums $\text{RbM}^{\text{III}}(\text{SO}_4)_2 \cdot 12\text{H}_2\text{O}$ ($\text{M}^{\text{III}} = \text{Al}, \text{Ga}, \text{In}, \text{Ti}, \text{V}, \text{Cr}, \text{Fe}$) between 275 and 1200 cm^{-1} : correlation between the electronic structure of the trivalent cation and structural abnormalities. *Inorg Chem* 35:5730–5736. <https://doi.org/10.1021/ic9602759>
- Wieczorek-Ciurowa K, Fela K, Kozak AJ (2001) Chromium(III)-ettringite formation and its thermal stability. *J Therm Anal Calorim* 65:655–660. <https://doi.org/10.1023/A:1017978414203>
- You K-S, Ahn J-W, Han D-Y, Cho K-H, Kim H (2007) Changing morphology and crystal structure in ettringite by trivalent chromium. *Mater Sci Forum* 544–545:529–532. <https://doi.org/10.4028/www.scientific.net/MSF.544-545.529>

Publisher's Note Springer Nature remains neutral with regard to jurisdictional claims in published maps and institutional affiliations.